Inorganic Chemistry

pubs.acs.org/IC Article

Magnetic Anisotropy: Structural Correlation of a Series of Chromium(II)−Amidinate Complexes

Yuan-Qi Zhai, Ning Ge, Zi-Han Li, Wei-Peng Chen, Tian Han, Zhong-Wen Ouyang, Zhenxing Wang,* and Yan-Zhen Zheng*

Cite This: *Inorg. Chem.* 2021, 60, 1344−1351 Read Online

ACCESS | Metrics & More | Article Recommendations | Supporting Information

ABSTRACT: Systematic substituent variations on amidinate ligands bring delicate changes of CrN_4 coordination in a family of chromium(II) complexes with the common formula of $Cr(RNC(CH_3)NR)_2$, where R = *i*Pr (**1**), Cy (**2**), Dipp (Dipp = 2, 6-diisopropylphenyl) (**3**), and *t*Bu (**4**). With the largest substituent group, **4** shows the largest distortion of the N_4 coordination geometry from square-planar to seesaw shape, which leads to its field-induced single-molecule magnet (SMM) behavior. This is an indication that **4** has the strongest axial magnetic anisotropy and/or optimized magnetic relaxation process. Combined with high-frequency/field electron paramagnetic resonance (HF-EPR) experiments and *ab initio* calculations, we deduce that the smallest energy gap between ground $^4\Psi_0$ and the first excited $^4\Psi_1$ orbitals in **4** contributes the most to its strongest magnetic anisotropy. Moreover, the lower *E* value of **4** ensures its being a field-induced SMM. Specifically, the *D* and *E* values were found to be correlated to the dihedral angle between the ΔN_1CrN_2 and ΔN_3CrN_4 triangles, indicating that distortion from ideal square-planar geometry to the seesaw help increase axial magnetic anisotropy and suppress the transversal part. Thus, the study on this system not only expands the family of Cr(II)-based SMMs but also contributes to a deeper understanding of magneto-structural correlation in four-coordinate Cr(II) SMMs.

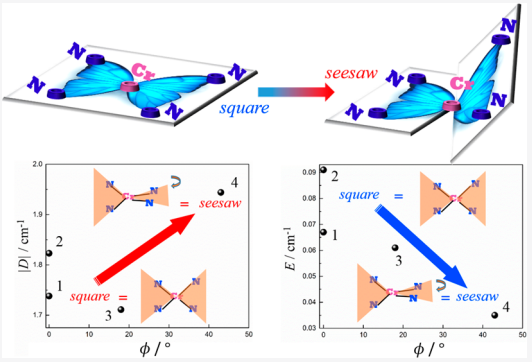

INTRODUCTION

Magneto-structure correlations which can guide the chemical synthesis for specific magnetism of coordination complexes are fundamentally important. As magnetic anisotropy is the decisive factor in making high-performance single-ion magnets (SIMs) or mononuclear single-molecule magnets (SMMs), the correlation between the structure and magnetic anisotropy of such complexes is crucial.[1−3] However, unambiguous magneto-structural correlation needs systematic study of a series of relevant complexes, which posts a challenge for synthetic chemists. So far, there are two geometries that are well understood. The first one is the linear two-coordinate geometry. These complexes, such as [(NHC)CoNDmp] (NHC = siPr, Dmp = 2,6-dimesitylphenyl),[4] $[Ni(MDABCO)_2Cl_3]ClO_4$ (MDABCO$^+$ = 1-methyl-4-aza-1 azoniabicyclo[2.2.2]octanium cation),[5] $\{[Fe(C(SiMe_3)_3)_2]^{0\text{ or }-1}\}$,[6,7] FeL_2 (L = $N(SiMe_3)$(Dipp), N(H)Ar′, N(H)Ar*),[6] and $[Co(C(SiMe_2ONaph)_3)_2]$[8] (Naph is a naphthyl group), show strong axial magnetic anisotropy, which means this coordination mode is suitable to enhance the axial magnetic anisotropy for metal ions such as iron(I or II), cobalt(II), and nickel(II). The other one is the four-coordinate geometry, but this is only for cobalt(II) complexes.[9,10] This geometry shows an intriguing maximized axial zero-field splitting parameter, the *D* value, at a 14−15° deviation from a tetrahedron.[10]

In contrast to cobalt(II)[8−12] and iron(I or II),[6,7,13−15] other 3d transition-metal-based SIMs are less systematically studied. Chromium, whose dominant isotopes have no nuclear spin, is very attractive. Until now, only a limited number of Cr(II) SMMs have been reported, including three multinuclear cluster SMMs, namely, $[Cr_5(tpda)_4Cl_2]$ (where H_2tpda = N^2,N^6-di(pyridin-2-yl)pyridine-2,6-diamine),[16] $\{SrCr_2(1,10\text{-phenanthroline})_2(C_2O_4)_4\}\cdot H_2O$, and $\{SrCr_2(2,2'\text{-bipyridine})_2(C_2O_4)_4(H_2O)\}\cdot 5H_2O$,[17] as well as two SIMs, namely, $[Cr(N(TMS)_2)_2(pyridine)_2]$ (TMS = $SiMe_3$), $[Cr(N(TMS)_2)_2(tetrahydrofuran)_2]$,[18] and $\{[(\eta^1\text{-N-3,5-}^t\text{Bu}_2\text{dp})_4Cr][(\eta^5\text{-(N,N,C,C,P)})_2\text{-K}(\eta^1\text{-O-THF})_2]_2\}$ (dp^- = 1,2-diaza-4-phospholide).[19] In this aspect, a study on Cr(II)-based SIMs would be very interesting.

Herein, we report four mononuclear Cr(II) amidinate complexes, namely, $Cr(i\text{PrNC}(CH_3)N i\text{Pr})_2$ (iPrNC(CH_3)-

Received: July 13, 2020
Published: January 11, 2021

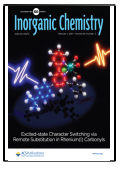

https://dx.doi.org/10.1021/acs.inorgchem.0c02065
Inorg. Chem. 2021, 60, 1344−1351

N*i*Pr = *N*,*N*′-diisopropylamidinate) **1**, Cr(CyNC(CH_3)NCy)$_2$ (CyNC(CH_3)NCy = *N*,*N*′-dicyclohexylamidinate) **2**, Cr(DippNC(CH_3)NDipp)$_2$ (DippNC(CH_3)NDipp = *N*,*N*′-bis(2,6-diisopropylphenyl)amidinate) **3**, and Cr(*t*BuNC(CH_3)N*t*Bu)$_2$ (*t*BuNC(CH_3)N*t*Bu = *N*,*N*′-di*tert*-butylamidinate) **4**. Each of the complexes feature a similar CrN_4 coordination environment. However, with the variation induced by different substituents, complex **4** with the largest *t*Bu group exhibits an obvious field-induced slow magnetic relaxation behavior. Further high-frequency/field electron paramagnetic resonance (HF-EPR) experiments and *ab initio* calculations indicate the largest axial magnetic anisotropy of **4** and reveal that the distortion from ideal square-planar geometry to the seesaw enhances the axial magnetic anisotropy in this series of Cr(II) complexes. Hence, a magneto-structural correlation of the magnetic anisotropy and the four coordinate Cr(II) with a N_4 first coordination sphere is elaborated in this work.

RESULTS AND DISCUSSION

Syntheses. The syntheses of the corresponding lithium salts, namely, [*i*PrNC(CH_3)N*i*Pr]Li(Et_2O), [CyNC(CH_3)NCy]Li(Et_2O), [DippNC(CH_3)NDipp]Li(Et_2O), and [*t*BuNC(CH_3)N*t*Bu]Li(Et_2O), are detailed in the Supporting Information (Scheme 1). Compounds **1**−**4** were obtained by

Scheme 1. Synthetic Route for Compounds 1−4

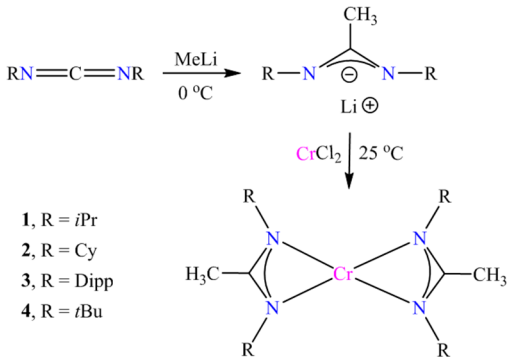

treatment of anhydrous $CrCl_2$ with the corresponding lithium salt (1:1) in THF, according to the literature-reported synthetic procedure.[20−22] All compounds were isolated as a crystalline solid crystallized in pentane at −35 °C (for details, see the Supporting Information).

Structures. Single-crystal X-ray diffraction analyses were performed, revealing that complex **1** crystallizes in triclinic space group $P\bar{1}$. The central Cr(II) ion displays a rectangular configuration with four N atoms of two [*i*PrNC(CH_3)N*i*Pr]$^-$ ligands coordinated in the equatorial plane (Figure 1a). The four Cr−N bond lengths are almost the same (ca. 2.08(1) Å), and the acute N−Cr−N angle averages at 63(1)°. The crystal packing diagram (Figure S1a) indicates that the shortest intermolecular separation among Cr(II) ions is 6.5 Å.

The crystal structure of complex **2** is similar to that of **1** but the crystal space group is different (monoclinic, $P2_1/c$). Two [CyNC(CH_3)NCy]$^-$ ligands are coordinated to the central Cr(II) ion, keeping four coordinated N atoms sharing the same plane with the Cr(II) ion (Figure 1b). The higher symmetry leads the Cr−N distances and the acute N−Cr−N angles to all be exactly the same (2.09(4) Å for the bonds and 64(0)° for the angles). The shortest Cr···Cr separation is 7.4 Å between neighboring molecules (Figure S1b).

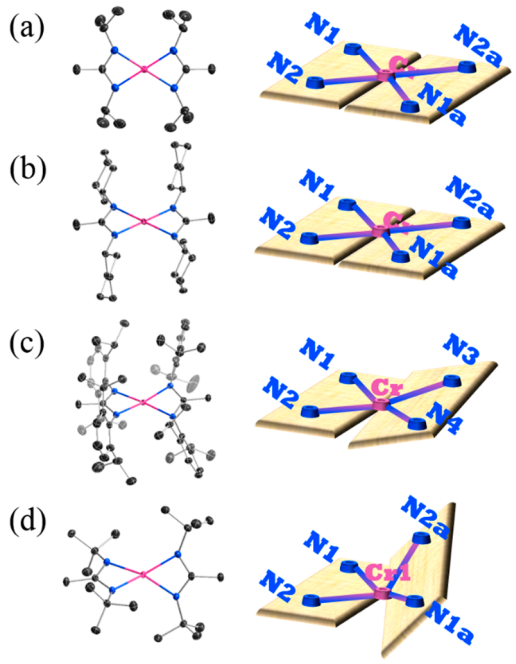

Figure 1. (Left) Molecular structures of **1**−**4** (a−d). Hydrogen atoms are not drawn for the sake of clarity. Color codes: Cr, pink; C, gray; N, blue. (Right) The diagrammatic sketch of CrN_4 geometry, and the atom positions correspond to the left ones.

Complex **3** crystallizes in same space group as complex **1** (Figure 1c). In this case, the Cr(II) ion and four N atoms are no longer coplanar, where the dihedral angle between the ΔN_1CrN_2 and ΔN_3CrN_4 triangles is 18(1)°, indicating the existence of a steric hindrance effect. The averaged bond length of Cr−N bonds is 2.05(1) Å, while the acute N−Cr−N angle is 64(1)°. The distance of the shortest intermolecular Cr···Cr separation is 10.9 Å (Figure S1c).

Complex **4** crystallizes in monoclinic space group $P2/n$, which is different from the above three complexes. Two independent molecules were localized into one unit cell (Figure 1d). For the first one, named by Cr1, owing to the further increase of steric hindrance by the -^{t}Bu substituent on the ligands, the dihedral angle between the ΔN_1Cr1N_2 and $\Delta N_{1a}Cr1N_{2a}$ triangles becomes larger, being 44(1)°. However, the average Cr1−N bond length (2.09(1) Å) and the acute N1−Cr1−N2 (N1a−Cr−N2a as well) angles (64(0)°) remain similar to those of compound **1**. For Cr2, the average Cr−N bond length and the acute N−Cr−N angle are 2.06(1) Å and 64(0)°, respectively, while the dihedral angle between the ΔN_3Cr2N_4 and $\Delta N_{3b}Cr2N_{4b}$ triangles remain nearly unchanged at 43(1)°. The distance of shortest intermolecular Cr···Cr separation is 7.7 Å (Figure S1d).

Magnetic Properties. Direct current (dc) susceptibility measurements were conducted on powder samples of complexes **1**−**4** under a 1000 Oe dc field and between 2 and 300 K (Figure S2). The room temperature $\chi_M T$ values are 3.05, 2.87, 2.77, and 2.87 cm^3 K mol^{-1} for **1**, **2**, **3**, and **4**, respectively. The values for the four complexes were consistent with the expected value 2.88 cm^3 K mol^{-1} calculated from a free high-spin Cr(II) ion with a *g* factor of 1.96. The $\chi_M T$ value decreases continuously upon cooling from 300 to 20 K, while below 20 K it meets a sharp drop. The low-temperature magnetization data (inset of Figure S2) for **1**−**4** are similar, where magnetization values continuously increase until 7 T

https://dx.doi.org/10.1021/acs.inorgchem.0c02065
Inorg. Chem. 2021, 60, 1344−1351

without saturation (the maximum values are 3.72, 3.43, 3.32, and 3.45 $N\beta$ for **1**−**4**, respectively), suggesting strong magnetic anisotropy for these complexes.

To gain the Landé factor (g), axial zero-field splitting (ZFS) parameter (D), and rhombic ZFS parameter (E) defined in the following spin Hamiltonian, we performed simulations on both magnetic susceptibility and magnetization plots using the program PHI.[23]

$$\hat{H} = D\left(\hat{S}_z^2 - \frac{1}{3}\hat{S}(\hat{S}+1)\right) + E(\hat{S}_x^2 - \hat{S}_y^2) + \mu_B g\hat{S}\cdot\vec{B} \quad (1)$$

The best simulations were yielded in Figure S2, with parameters listed in Table 1.

Table 1. Spin Hamiltonian Parameters from the Fitting of Magnetic Properties

	D (cm^{-1})	E (cm^{-1})	g_{iso}	χ_{TIP}[a] (cm^3 mol^{-1})
1	−2.1(6)	0.1(4)	1.99(7)	1.1×10^{-3}
2	−2.2(5)	0.1(4)	1.96(5)	3.6×10^{-4}
3	−2.2(2)	0.0(1)	1.91(1)	4.5×10^{-4}
4	−2.7(1)	0.0(1)	1.89(1)	6.3×10^{-4}

[a] χ_{TIP} represents temperature-independent paramagnetic component.

The D values for **1**−**3** are much smaller than that of **4**, whereas the E value of **4** is the smallest in the whole system. Here, the obtained ZFS parameters are close to our previously reported square-planar Cr(II)-based single-ion magnets (SIMs).[18] Meanwhile, the attempt of using positive D values in fitting was unsuccessful.

Ac magnetic susceptibility measurements were performed on investigating the dynamic magnetic relaxation of **1**−**4** (Figures 2, S3, and S4). In the absence of a dc applied field, no signals of χ'' ac susceptibility appear for all the four complexes, indicating a high quantum tunnelling of magnetization (QTM) rate.[24] Then frequency-dependent ac measurements were carried out under various magnetic fields. However, there was no improvement for **1**−**3** under the magnetic field range of 0−5000 Oe (Figure S4). While an optimum field of 3000 Oe was found for **4** to significantly suppress the QTM effect (Figure 2). The generalized Debye model was applicable for the fitting of Cole−Cole plots for **4**, which reveal the distribution of relaxation times (τ). The ln (τ) vs $1/T$ plot shows a nice linear relationship, and thus, only Orbach process was considered in the fitting. Using the equation $\tau^{-1} = \tau_0^{-1}\exp(-U_{eff}/k_BT)$ the effective energy barrier (U_{eff}) and the prefactor τ_0 were then determined as 8(2) K and $9(4) \times 10^{-6}$ s, respectively.

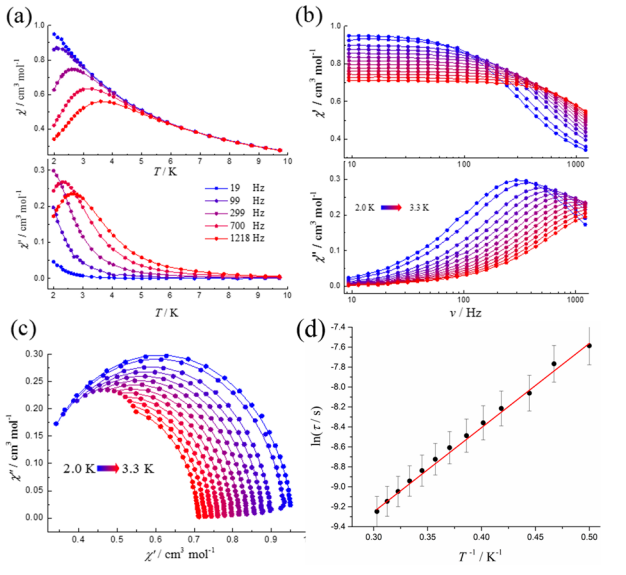

Figure 2. Temperature (a) and frequency (b) dependence of the in-phase (χ') and out-of-phase (χ'') ac susceptibility and Cole−Cole plots (c) under a 3000 Oe applied dc field for **4**. The solid lines are guides for the eyes. (d) The corresponding relaxation times for **4**.

HF-EPR Studies. Multifrequency HF-EPR experiments at 4.2 K were performed on samples **1**−**4** (details are in the Supporting Information). Figure S5 shows the raw HF-EPR spectra of polycrystalline powder samples of **1**−**4**. The HF-EPR spectra in the frequency limited up to 448 GHz were observed with strong resonances though some shaky waves were present in the plots due to the small amount of samples. The obtained variable-frequency resonance results were plotted in Figure 3 (left) as resonant field (H) vs frequency (ν) 2D plots. To investigate the ZFS parameters from the above-mentioned spin Hamiltonian, we first need to distinguish the allowed ($|\Delta M_s| = 1$) transitions from the nominally forbidden ($|\Delta M_s| > 1$) ones.[25] Such 2D map was previously obtained in other d^4 systems.[26]

Then, a least-squares fit was used for simulating to the in-phase HF-EPR resonances, with the resulted parameters listed in Table 2.

Moreover, the sign of D values can be confirmed by performing the simulating of HF-EPR spectra at selected frequency for each complex (Figure 3 (right)). It is found that, in all cases, negative D values reproduced better simulation curves to the experimental plots than positive ones.

To further assign the location of spin states and state transitions between them, we plot the Zeeman splitting diagrams for the complexes **1**−**4** (Figure 4) in three orthogonal directions where the z direction represents the principal ZFS axis. Along the z direction, a strong EPR signal was observed at 2.77 T (for selected 230 GHz frequency), 0.22 T (at 170 GHz frequency), 3.38 T (at 250 GHz frequency), and for **1**−**4**, respectively. Such an obvious signal was corresponding to the energy transition of $|2, -2\rangle \rightarrow |2, -1\rangle$ states (where the state represents $|S, M_s\rangle$). Besides this, a very weak EPR signal was found for **4** at 10.32 T owing to a $|2, 0\rangle \rightarrow |2, 1\rangle$ transition between excited states but with relatively low occupancy. Along the x direction, more than one resonance was found for all complexes. For **1**, the subsequent resonances at 7.09 and 10.79 T can be attributed to the energy transition of $|2, -1\rangle \rightarrow |2, +1\rangle$ and $|2, -2\rangle \rightarrow |2, +2\rangle$. For **2**, when $B\|x$, four resonances were observed almost in the same resonant magnetic field (1.87, 4.79, 6.63, and 9.34 T), referring to $|2, -1\rangle \rightarrow |2, 0\rangle$, $|2, -1\rangle \rightarrow |2, +1\rangle$, $|2, +2\rangle \rightarrow |2, -1\rangle$, and $|2, -2\rangle \rightarrow |2, +2\rangle$, respectively. For **3**, when $B\|x$, three resonances (6.86, 8.92, and 11.96 T) were observed referring to $|2, -2\rangle \rightarrow |2, +2\rangle$, $|2, +2\rangle \rightarrow |2, -1\rangle$, and $|2, -1\rangle \rightarrow |2, +1\rangle$. For **4**, when $B\|x$, two resonances (9.25 and 12.09 T) were observed referring to $|2, -2\rangle \rightarrow |2, +2\rangle$ and $|2, +2\rangle \rightarrow |2, -1\rangle$. Along the y direction, more than one resonance was found for all complexes. Along the y direction, situations were similar to the x direction. For **1**, transitions at 7.04, 8.98, and 11.51 T were viewed as energy transitions of $|2, -1\rangle \rightarrow |2, +1\rangle$, $|2, +2\rangle \rightarrow |2, -1\rangle$, and $|2, -2\rangle \rightarrow |2, +2\rangle$, respectively. For **2**, when $B\|y$, four resonances were found at the similar positions as those

https://dx.doi.org/10.1021/acs.inorgchem.0c02065
Inorg. Chem. 2021, 60, 1344−1351

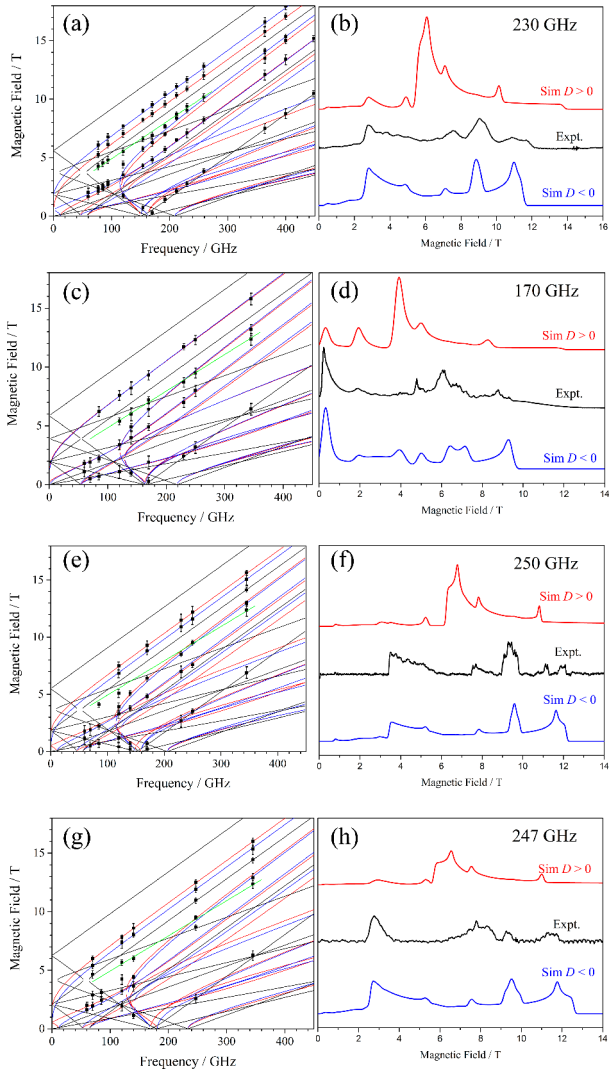

Figure 3. (Left) H vs ν plots at EPR transitions for **1** (a), **2** (c), **3** (e), and **4** (g) at 4.2 K. The squares stand for experimental data with error bars. Black, red, and blue curves are simulation lines to the experimentally determined EPR transition points along the magnetic field B following the x, y, and z directions, respectively. The green curves represent resonances from off-axis transitions. (Right) Experimental spectrum (black traces) of **1** (b), **2** (d), **3** (f), and **4** (h) at selected frequencies. Red and blue curves are simulated plots using positive and negative D values, respectively.

Table 2. Spin Hamiltonian Parameters from the Fitting of HF-EPR Spectra

	D (cm^{-1})	E (cm^{-1})	g_x	g_y	g_z
1	−1.74(13)	0.07(4)	1.98(2)	1.96(3)	2.00(1)
2	−1.82(17)	0.09(3)	1.97(2)	1.97(2)	2.00(1)
3	−1.71(11)	0.06(3)	1.98(3)	1.97(2)	2.00(1)
4	−1.94(10)	0.03(5)	1.98(2)	1.96(1)	2.00(1)

in $B\|\|x$, referring to $|2,-1\rangle \rightarrow |2,0\rangle$, $|2,-1\rangle \rightarrow |2,+1\rangle$, $|2,+2\rangle \rightarrow |2,-1\rangle$, and $|2,-2\rangle \rightarrow |2,+2\rangle$, respectively. For **3**, only one resonance at a magnetic field of 11.00 T for $B\|\|y$ belonged to $|2,-2\rangle \rightarrow |2,+2\rangle$. For **4**, the transition for $B\|\|y$ at 11.35 T belonged to $|2,-2\rangle \rightarrow |2,+2\rangle$.

The negative D values of **1**−**4** indicated their uniaxial type magnetic anisotropy, and **4** possessed the largest magnitude. Here, we can rationalize a much lower E value for **4**.

Computational Studies. The *ab initio* calculations with CASSCF/NEVPT2 protocol implemented in Orca 4.0 were performed to study the magnetic anisotropy of transition metal ions on **1**−**4**.[27] The X-ray crystallographically determined structures were directly used for calculations. The ZFS parameters have been calculated, showing negative D values for **1**−**4** (Table 3), which agree well with the experimental results.[28]

To determine the D values, the following equation was used:

$$D = \frac{4}{9}\zeta_{\text{eff}}^2\left[\frac{1}{\Delta(^4\Psi_0 - {}^4\Psi_2)} - \frac{1}{\Delta(^4\Psi_1 - {}^4\Psi_0)}\right] \quad (2)$$

Equation 2 indicates that the magnetic anisotropy is arising from the energy gap between the low-lying first excited state ($^4\Psi_1$) and the second excited state ($^4\Psi_2$). For **1**, the $^4\Psi_1$ and $^4\Psi_2$ states lie at 16359.7 and 17108.5 cm^{-1} above the ground state ones. The contribution to the negative D values that comes from the $^4\Psi_1$ state is −0.78 cm^{-1}, while from the $^4\Psi_2$ state is −0.70 cm^{-1}, indicating that the energy gap between the ground state and two low-lying excited states determine the axial magnetic anisotropy in **1**.

For **2** and **3**, the situations are similar, where energies (in cm^{-1}) of $^4\Psi_1$ and $^4\Psi_2$ states are 19142.6 and 19701.6 for **2** and are 18906.4 and 19100.6, for **3**, respectively. The contributions of D values from the former one are −0.74 and −0.76 cm^{-1} while they are −0.70 and −0.68 cm^{-1} from the latter one, for **2** and **3**, respectively. For **4**, the results for two individual Cr1 and Cr2 sites are similar due to similar coordination geometries. The magnitude of the axial ZFS parameter of Cr1 (Cr2) is much larger than that for the other three complexes, which is mainly due to the stronger contribution from the first excited quintet state with −0.97 (−1.04) cm^{-1}. Meanwhile, the $^4\Psi_1$ state is much lower than the others, which contributes to the stronger magnetic anisotropy to **4** according to eq 2. Compared to **1**−**3**, the most relevant factor is the coordination geometry of the central Cr(II) ion. In this case, the obvious lower-lying $^4\Psi_1$ state in **4** is owed to the more dramatic structure distortion from square-planar to seesaw type. Such a magneto-structural correlation proposed here is somehow similar to a previously reported CoN_4 system.[9]

As presented in Figure 5, the five active orbitals of **4** are mostly constructed by 3d-orbitals of the central Cr(II) ion together with slight contributions from coordinated ligands. The situations are similar for other three complexes (Figures S7−S9). To further analyze the *ab initio* wave functions, we deduce a clear connection between the spin excitation among 3d-orbitals and the energy gaps of states, which is suitable for 3d transition-ion-based SIM systems. In the case of $^4\Psi_0$ and $^4\Psi_1$, the $d_{x^2-y^2} \rightarrow d_{yz}$ transition is responsible for the energy difference of such states and contributes to the negative D values. In case of the $d_{z^2} \rightarrow d_{yz}$ transition, on the contrary, it contributes to the positive D values. Taken together, we can see that the energy gap between $^4\Psi_0$ and $^4\Psi_1$ states offers a negative D value, resulting in the axial magnetic anisotropy of **1**−**4**.[29]

Based on the above results, we are able to explain the reason why complex **4** is a field-induced SIM while others are not. The most obvious difference on **4** is that E value, which is much smaller than those of **1**−**3**, leading to lower strength of the QTM, as proven by both *ab initio* calculation and EPR simulations. The average Cr−N bond lengths for **1**−**4** range from 2.05−2.09 Å while the N1−Cr−N2 angles range from

https://dx.doi.org/10.1021/acs.inorgchem.0c02065
Inorg. Chem. 2021, 60, 1344−1351

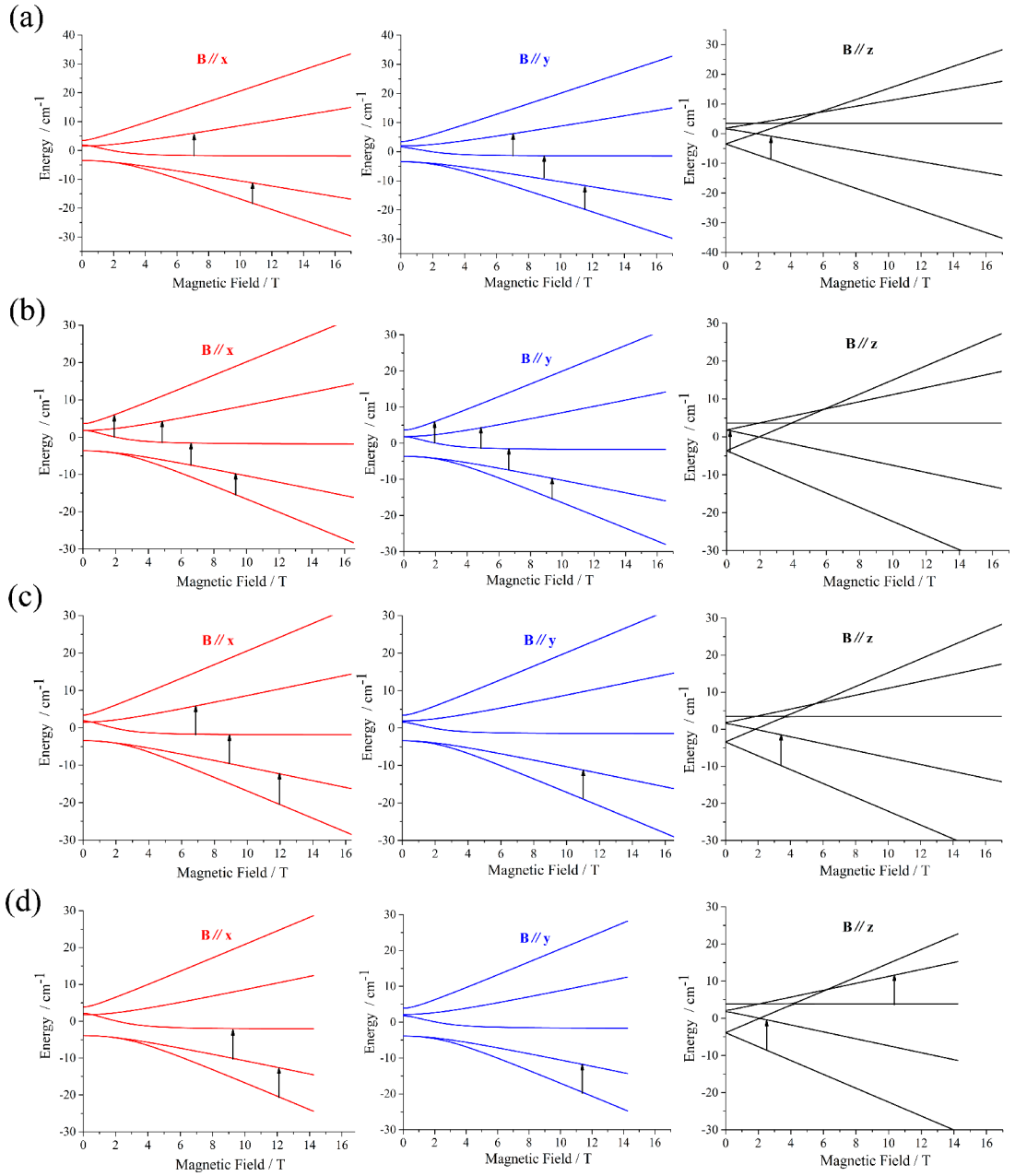

Figure 4. Magnetic field-dependent energy levels for **1**–**4** (a–d) in the *xyz* directions where the *z* orientation represents the principal ZFS axis. Arrows stand for EPR transitions along *x* (red), *y* (blue), and *z* (black) in a selected frequency.

Table 3. Parameters of ORCA CASSCF+NEVPT2 Calculations for 1–4

		1	2	3	4(Cr1)	4(Cr2)
D (cm^{-1}) E/D		−1.50	−1.47	−1.48	−1.68	−1.71
		0.02	0.02	0.02	0.00	0.00
S = 2	g_x	1.98	1.98	1.98	1.93	1.93
	g_y	1.99	1.99	1.99	1.95	1.95
	g_z	1.99	1.99	1.99	2.00	2.00

63–64°, which do not exhibit much difference. However, the dihedral angles, defined by the angle between ΔN_1CrN_2 and $\Delta N_{1a}CrN_{2a}$ triangles (ϕ), show obvious distinction from zero for **1** and **2** to 42° for **4**. Thus, we developed a magneto-structure correlation between this dihedral angle and ZFS parameters (D and E values from HF-EPR simulations) and plotted the correlation in Figure 6. When ϕ is zero, the magnitude of D value is the smallest and that of E value is the largest. Upon increasing ϕ from 0 to 42°, i.e., varying the coordination geometry from square to seesaw, D values increase steadily by 13% and E values decrease sharply by 66%. Hence, we deduced that four-coordinate Cr(II) complexes with the seesaw geometry can dramatically lift the magnitude of D value while reducing the E value, resulting in a good SMM candidate. The tendency is obvious, but we cannot obtain quantitative correlations.

CONCLUSIONS

By using four amidinate ligands we systematically studied the peripheral substituents on magneto-structure correlations of a series of Cr(II) complexes with a similar CrN_4 coordination environment but different degree of distortion away from the

https://dx.doi.org/10.1021/acs.inorgchem.0c02065
Inorg. Chem. 2021, 60, 1344–1351

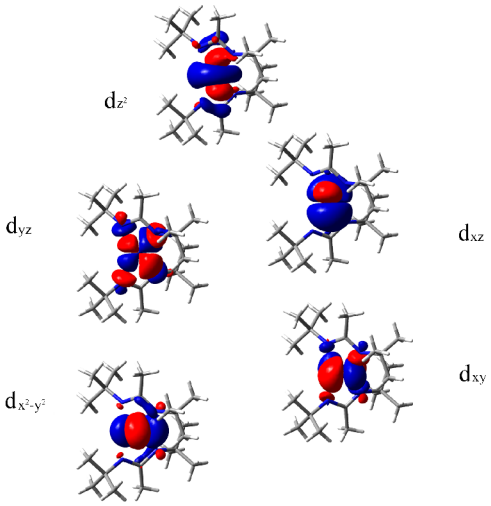

Figure 5. NEVPT2 computed active orbital energy orderings for the lowest-lying quintet state for **4**.

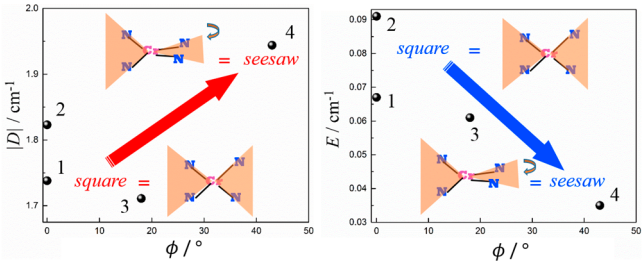

Figure 6. Correlation of dihedral angle (ϕ) between the ΔN_1CrN_2 and ΔN_3CrN_4 triangles with D (left) and E (right) values from HF-EPR simulations (black dots). The parameters for **4** are averaged from those of Cr(1) and Cr(2).

rectangular geometry. Magnetic measurements show that only the largest distorted complex, namely, **4**, shows field-dependent SIM behaviors. The HF-EPR study shows a relatively lower transversal contribution of ZFS parameter for **4**. Combined with *ab initio* calculation results, we find that the smaller energy gap between $^4\Psi_0$ and $^4\Psi_1$ orbitals leads to the largest negative D value for **4**, while the smaller E value enhances its field-induced SIM behavior. Finally, the qualitative magneto-structure correlations between $E(\phi)$ and ZFS have been elaborated, indicating that the geometry distortion from square to seesaw tends to diminish the transversal magnetic anisotropy of the Cr(II) ion.

■ ASSOCIATED CONTENT

Supporting Information

The Supporting Information is available free of charge at https://pubs.acs.org/doi/10.1021/acs.inorgchem.0c02065.

Crystallographic data (Table S1), bond distances and angles (Table S2), magnetic relaxation data (Table S3), *ab initio* calculation data (Tables S4−S6); crystallographic packing plots (Figure S1), static magnetic data (Figure S2), dynamic magnetic data (Figures S3 and S4), HF-EPR spectra (Figures S5 and S6), and NEVPT2 computed active orbitals (Figures S7−S9) (PDF)

Accession Codes

CCDC 2011865−2011868 contain the supplementary crystallographic data for this paper. These data can be obtained free of charge via www.ccdc.cam.ac.uk/data_request/cif, or by emailing data_request@ccdc.cam.ac.uk, or by contacting The Cambridge Crystallographic Data Centre, 12 Union Road, Cambridge CB2 1EZ, UK; fax: +44 1223 336033.

■ AUTHOR INFORMATION

Corresponding Authors

Yan-Zhen Zheng − *Xi'an Jiaotong University Shenzhen Research School, Frontier Institute of Science and Technology (FIST), State Key Laboratory for Mechanical Behavior of Materials, MOE Key Laboratory for Nonequilibrium Synthesis of Condensed Matter, Xi'an Key Laboratory of Sustainable Energy and Materials Chemistry and School of Chemistry, Xi'an Jiaotong University, Xi'an 710054, China;* orcid.org/0000-0003-4056-097X; Email: zheng.yanzhen@xjtu.edu.cn

Zhenxing Wang − *Wuhan National High Magnetic Field Centre & School of Physics, Huazhong University of Science and Technology, Wuhan 430074, China;* orcid.org/0000-0003-2199-4684; Email: zxwang@hust.edu.cn

Authors

Yuan-Qi Zhai − *Xi'an Jiaotong University Shenzhen Research School, Frontier Institute of Science and Technology (FIST), State Key Laboratory for Mechanical Behavior of Materials, MOE Key Laboratory for Nonequilibrium Synthesis of Condensed Matter, Xi'an Key Laboratory of Sustainable Energy and Materials Chemistry and School of Chemistry, Xi'an Jiaotong University, Xi'an 710054, China*

Ning Ge − *Xi'an Jiaotong University Shenzhen Research School, Frontier Institute of Science and Technology (FIST), State Key Laboratory for Mechanical Behavior of Materials, MOE Key Laboratory for Nonequilibrium Synthesis of Condensed Matter, Xi'an Key Laboratory of Sustainable Energy and Materials Chemistry and School of Chemistry, Xi'an Jiaotong University, Xi'an 710054, China*

Zi-Han Li − *Xi'an Jiaotong University Shenzhen Research School, Frontier Institute of Science and Technology (FIST), State Key Laboratory for Mechanical Behavior of Materials, MOE Key Laboratory for Nonequilibrium Synthesis of Condensed Matter, Xi'an Key Laboratory of Sustainable Energy and Materials Chemistry and School of Chemistry, Xi'an Jiaotong University, Xi'an 710054, China*

Wei-Peng Chen − *Xi'an Jiaotong University Shenzhen Research School, Frontier Institute of Science and Technology (FIST), State Key Laboratory for Mechanical Behavior of Materials, MOE Key Laboratory for Nonequilibrium Synthesis of Condensed Matter, Xi'an Key Laboratory of Sustainable Energy and Materials Chemistry and School of Chemistry, Xi'an Jiaotong University, Xi'an 710054, China*

Tian Han − *Xi'an Jiaotong University Shenzhen Research School, Frontier Institute of Science and Technology (FIST), State Key Laboratory for Mechanical Behavior of Materials, MOE Key Laboratory for Nonequilibrium Synthesis of Condensed Matter, Xi'an Key Laboratory of Sustainable Energy and Materials Chemistry and School of Chemistry, Xi'an Jiaotong University, Xi'an 710054, China;* orcid.org/0000-0002-8753-7999

Zhong-Wen Ouyang − *Wuhan National High Magnetic Field Centre & School of Physics, Huazhong University of Science and Technology, Wuhan 430074, China*

Complete contact information is available at: https://pubs.acs.org/10.1021/acs.inorgchem.0c02065

https://dx.doi.org/10.1021/acs.inorgchem.0c02065
Inorg. Chem. 2021, 60, 1344−1351

Notes

The authors declare no competing financial interest.

■ ACKNOWLEDGMENTS

This work was supported by the Shenzhen Science and Technology Program (JCYJ20180306170859634), the National Natural Science Foundation of China (21701046, 21773130, 21801202, and 21971203), the Shaanxi National Science Foundation (2019JQ-016), the China Postdoctoral Science Foundation (2019T120891 and 2018M643615), the Key Laboratory Construction Program of Xi'an Municipal Bureau of Science and Technology (201805056ZD7CG40), the Key Scientific and Technological Innovation Team of Shaanxi Province (2020TD-001), the Cyrus Chung Ying Tang Foundation, and the Fundamental Research Funds for Central Universities.

■ REFERENCES

(1) Craig, G. A.; Murrie, M. 3d single-ion magnets. *Chem. Soc. Rev.* **2015**, *44*, 2135−2147.
(2) Gomez-Coca, S.; Aravena, D.; Morales, R.; Ruiz, E. Large magnetic anisotropy in mononuclear metal complexes. *Coord. Chem. Rev.* **2015**, *289*, 379−392.
(3) Frost, J. M.; Harriman, K. L. M.; Murugesu, M. The rise of 3-d single-ion magnets in molecular magnetism: towards materials from molecules? *Chem. Sci.* **2016**, *7*, 2470−2491.
(4) Yao, X.-N.; Du, J.-Z.; Zhang, Y.-Q.; Leng, X.-B.; Yang, M.-W.; Jiang, S.-D.; Wang, Z.-X.; Ouyang, Z.-W.; Deng, L.; Wang, B.-W.; Gao, S. Two-Coordinate Co(II) Imido Complexes as Outstanding Single-Molecule Magnets. *J. Am. Chem. Soc.* **2017**, *139*, 373−380.
(5) Marriott, K. E. R.; Bhaskaran, L.; Wilson, C.; Medarde, M.; Ochsenbein, S. T.; Hill, S.; Murrie, M. Pushing the limits of magnetic anisotropy in trigonal bipyramidal Ni(ii). *Chem. Sci.* **2015**, *6*, 6823−6828.
(6) Zadrozny, J. M.; Atanasov, M.; Bryan, A. M.; Lin, C.-Y.; Rekken, B. D.; Power, P. P.; Neese, F.; Long, J. R. Slow magnetization dynamics in a series of twocoordinate iron(II) complexes. *Chem. Sci.* **2013**, *4*, 125−138.
(7) Zadrozny, J. M.; Xiao, D. J.; Atanasov, M.; Long, G. J.; Grandjean, F.; Neese, F.; Long, J. R. Magnetic blocking in a linear iron(I) complex. *Nat. Chem.* **2013**, *5*, 577−581.
(8) Bunting, P. C.; Atanasov, M.; Damgaard-Møller, E.; Perfetti, M.; Crassee, I.; Orlita, M.; Overgaard, J.; van Slageren, J.; Neese, F.; Long, J. R. A linear cobalt(II) complex with maximal orbital angular momentum from a non-Aufbau ground state. *Science* **2018**, *362*, eaat7319.
(9) Zadrozny, J. M.; Telser, J.; Long, J. R. Slow magnetic relaxation in the tetrahedral cobalt(II) complexes $[Co(EPh)_4]^{2-}$ (E = O, S, Se). *Polyhedron* **2013**, *64*, 209−217.
(10) Wu, T.; Zhai, Y.−Q.; Deng, Y.-F.; Chen, W.-P.; Zhang, T.; Zheng, Y.-Z. Correlating magnetic anisotropy with the subtle coordination geometry variation of a series of cobalt(ii)-sulfonamide complexes. *Dalton Trans.* **2019**, *48*, 15419−15426.
(11) Rechkemmer, Y.; Breitgoff, F. D.; van der Meer, M.; Atanasov, M.; Hakl, M.; Orlita, M.; Neugebauer, P.; Neese, F.; Sarkar, B.; van Slageren, J. A four-coordinate cobalt(II) single-ion magnet with coercivity and a very high energy barrier. *Nat. Commun.* **2016**, *7*, 10467−10474.
(12) (a) Tu, D.-S.; Shao, D.; Yan, H.; Lu, C.-S. A carborane-incorporated mononuclear Co(ii) complex showing zero-field slow magnetic relaxation. *Chem. Commun.* **2016**, *52*, 14326−14329. (b) Alcoba, D. R.; Oña, O. B.; Massaccesi, G. E.; Torre, A.; Lain, L.; Melo, J. I.; Peralta, J. E.; Oliva-Enrich, J. M. Magnetic Properties of Mononuclear Co(II) Complexes with Carborane Ligands. *Inorg. Chem.* **2018**, *57*, 7763−7769.
(13) Harman, W. H.; Harris, T. D.; Freedman, D. E.; Fong, H.; Chang, A.; Rinehart, J. D.; Ozarowski, A.; Sougrati, M. T.; Grandjean, F.; Long, G. J.; Long, J. R.; Chang, C. J. Slow Magnetic Relaxation in a Family of Trigonal Pyramidal Iron(II) Pyrrolide Complexes. *J. Am. Chem. Soc.* **2010**, *132*, 18115−18126.
(14) Freedman, D. E.; Harman, W. H.; Harris, T. D.; Long, G. J.; Chang, C. J.; Long, J. R. Slow Magnetic Relaxation in a High-Spin Iron(II) Complex. *J. Am. Chem. Soc.* **2010**, *132*, 1224−1225.
(15) Lin, P.-H.; Smythe, N. C.; Gorelsky, S. I.; Maguire, S.; Henson, N. J.; Korobkov, I.; Scott, B. L.; Gordon, J. C.; Baker, R. T.; Murugesu, M. Importance of Out-of-State Spin−Orbit Coupling for Slow Magnetic Relaxation in Mononuclear FeII Complexes. *J. Am. Chem. Soc.* **2011**, *133*, 15806−15809.
(16) Cornia, A.; Rigamonti, L.; Boccedi, S.; Clerac, R.; Rouzieres, M.; Sorace, L. Magnetic blocking in extended metal atom chains: a pentachromium(ii) complex behaving as a single-molecule magnet. *Chem. Commun.* **2014**, *50*, 15191−15194.
(17) Androš Dubraja, L.; Jurić, M.; Popović, J.; Pajić, D.; Krupskaya, Y.; Kataev, V.; Buchner, B.; Žilić, D. Magneto-structural correlations in oxalatebridged Sr(II)Cr(III) coordination polymers: structure, magnetization, X-band, and high-field ESR studies. *Dalton Trans.* **2018**, *47*, 3992−4000.
(18) Deng, Y. F.; Han, T.; Wang, Z. X.; Ouyang, Z. W.; Yin, B.; Zheng, Z. P.; Krzystek, J.; Zheng, Y. Z. Uniaxial magnetic anisotropy of square-planar chromium(ii) complexes revealed by magnetic and HF-EPR studies. *Chem. Commun.* **2015**, *51*, 17688−17691.
(19) Su, J.; Yin, L.; Ouyang, Z.; Wang, Z.; Zheng, W. 1,2-Diaza-4-phospholide complexes of chromium(II): dipotassium organochromates behaving as single-molecule magnets. *Dalton Trans.* **2020**, *49*, 6945−6949.
(20) Coles, M. P.; Swenson, D. C.; Jordan, R. F.; Young, V. G. Synthesis and Structures of Mono- and Bis(amidinate) Complexes of Aluminum. *Organometallics* **1997**, *16*, 5183−5194.
(21) Sadique, A. R.; Heeg, M. J.; Winter, C. H. A Weak, Short Metal-Metal Bond in a Chromium(II) Amidinate Complex. *J. Am. Chem. Soc.* **2003**, *125*, 7774−7775.
(22) Shoukang, H.; Gambarotta, S.; Bensimon, C.; Edema, J. J.H. Ligand steric bulk: A neglected factor in the formation of Cr-Cr supershort contacts. *Inorg. Chim. Acta* **1993**, *213*, 65−74.
(23) Chilton, N. F.; Anderson, R. P.; Turner, L. D.; Soncini, A.; Murray, K. S. PHI: A powerful new program for the analysis of anisotropic monomeric and exchange-coupled polynuclear d- and f-block complexes. *J. Comput. Chem.* **2013**, *34*, 1164−1175.
(24) Carlin, R. L.; van Duyneveldt, A. J. *Magnetic Properties of Transition Metal Compounds*; Springer: New York, 1976.
(25) Smith, G. M.; Riedi, P. C.; Gilbert, B. C.; Davies, M. J.; Murphy, D. M. *Electron Paramagnetic Resonance*; Royal Society of Chemistry: Cambridge, U.K., 2002; pp 254−303.
(26) Vallejo, J.; Pascual-Alvarez, A.; Cano, J.; Castro, I.; Julve, M.; Lloret, F.; Krzystek, J.; De Munno, G.; Armentano, D.; Wernsdorfer, W.; Ruiz-Garcia, R.; Pardo, E. Field-Induced Hysteresis and Quantum Tunneling of the Magnetization in a Mononuclear Manganese(III) Complex. *Angew. Chem.* **2013**, *125*, 14325−14329.
(27) (a) Malmqvist, P. A.; Roos, B. O. The CASSCF state interaction method. *Chem. Phys. Lett.* **1989**, *155*, 189−194. (b) Roos, B. O.; Taylor, P. R.; Sigbahn, P. E.M. A complete active space SCF method (CASSCF) using a density matrix formulated super-CI approach. *Chem. Phys.* **1980**, *48*, 157−173. (c) Angeli, C.; Cimiraglia, R.; Malrieu, J. P. N-electron valence state perturbation theory: a fast implementation of the strongly contracted variant. *Chem. Phys. Lett.* **2001**, *350*, 297−305. (d) Angeli, C.; Cimiraglia, R.; Evangelisti, S.; Leininger, T.; Malrieu, J. P. Introduction of *n*-electron valence states for multireference perturbation theory. *J. Chem. Phys.* **2001**, *114*, 10252−10264.
(28) (a) Chibotaru, L. F.; Ungur, L. *Ab initio* calculation of anisotropic magnetic properties of complexes. I. Unique definition of pseudospin Hamiltonians and their derivation. *J. Chem. Phys.* **2012**, *137*, 064112.
(29) Deng, Y.-F.; Han, T.; Yin, B.; Zheng, Y.-Z. On balancing the QTM and the direct relaxation processes in single-ion magnets − the

https://dx.doi.org/10.1021/acs.inorgchem.0c02065
Inorg. Chem. 2021, 60, 1344−1351

importance of symmetry control. *Inorg. Chem. Front.* **2017**, *4*, 1141−1148.

https://dx.doi.org/10.1021/acs.inorgchem.0c02065
Inorg. Chem. 2021, 60, 1344−1351